# High-throughput search for magnetic topological materials using spin-orbit spillage, machine learning, and experiments

Kamal Choudhary [1,2,*] Kevin F. Garrity,[1] Nirmal J. Ghimire,[3,4] Naween Anand [5] and Francesca Tavazza[1]

[1]*Materials Science and Engineering Division, National Institute of Standards and Technology, Gaithersburg, Maryland 20899, USA*
[2]*Theiss Research, La Jolla, California 92037, USA*
[3]*Department of Physics and Astronomy, George Mason University, Fairfax, Virginia 22030, USA*
[4]*Quantum Science and Engineering Center, George Mason University, Fairfax, Virginia 22030, USA*
[5]*Materials Science Division, Argonne National Laboratory, Argonne, Illinois 60439, USA*

Magnetic topological insulators and semimetals have a variety of properties that make them attractive for applications, including spintronics and quantum computation, but very few high-quality candidate materials are known. In this paper, we use systematic high-throughput density functional theory calculations to identify magnetic topological materials from the $\approx 40\,000$ three-dimensional materials in the JARVIS-DFT database. First, we screen materials with net magnetic moment $>0.5\,\mu B$ and spin-orbit spillage (SOS) $>0.25$, resulting in 25 insulating and 564 metallic candidates. The SOS acts as a signature of spin-orbit-induced band-inversion. Then we carry out calculations of Wannier charge centers, Chern numbers, anomalous Hall conductivities, surface band structures, and Fermi surfaces to determine interesting topological characteristics of the screened compounds. We also train machine learning models for predicting the spillages, band gaps, and magnetic moments of new compounds, to further accelerate the screening process. We experimentally synthesize and characterize a few candidate materials to support our theoretical predictions.

## I. INTRODUCTION

The interplay of topology [1,2] and electronic band structures in nonmagnetic materials has led to several material categories, most notably topological insulators (TIs) [1,3], Dirac semimetals (SMs), and broken-inversion Weyl SMs [4,5], topological crystalline insulators [6], nodal line SMs [7,8]. However, many potentially useful quantum effects [9–12,13], like anomalous Hall conductivity (AHC), are only possible in topological materials with broken time reversal symmetry, including exotic phases such as Chern insulators [9,14], magnetic axion insulators [9,15], and magnetic SMs (MSMs) [16]. Experiments such as AHC [17], spin-Seebeck [18], spin-torque ferromagnetic resonance (FMR) [19] and angle-resolved photoemission spectroscopy (ARPES) [20], Fourier transform scanning tunneling spectroscopy [21], and Shubnikov de Haas oscillations can be useful for analyzing the topological behavior. Only a few such materials are reported experimentally, and many of those materials are limited to very low temperatures or have trivial bands that overlap with the topological band features, limiting their utility. There is a significant opportunity to find more robust magnetic topological materials and to further our understanding of the underlying mechanisms leading to their topological properties.

A common feature of many topological material classes is the presence of spin-orbit-induced band inversion, where the inclusion of spin-orbit coupling (SOC) in a calculation causes the character of the occupied wave functions at a k-point to change. Spin-orbit spillage (SOS) [22–24] is a method to measure this band inversion by comparing the wave functions with and without SOC. SOS is based on density functional theory (DFT) calculations-based wave function analysis and has been proven to be a useful technique for finding topological materials. Previous studies [22–24] have looked at three-dimensional (3D) nonmagnetic materials as well as two-dimensional (2D) materials with and without magnetism. Due to its ease of calculation, without any need for symmetry analysis or dense k-point interpolation, SOS is an excellent tool for identifying candidate materials to many topological phases. Advantages of this technique include that it can apply to materials with low or no symmetries, including disordered or defective materials, and that it can identify the fundamental driver of topological behavior, the band inversion, even if the exact topological classification of a material depends on detailed features like the exact magnetic ordering, spin direction, or sample thickness. After identifying high-SOS materials, further analysis is necessary to identify the specific topological phases that may arise from the band inversion.

Stoichiometric magnetic TIs (MTIs) are very rare. $MnBi_2Te_3$ [25–28], an antiferromagnetic TI, is one of the most studied and well-characterized examples of a 3D MTI, and thin films of $MnBi_2Te_3$ exhibit quantized AHC [25,26]. Several MSMs, such as CuMnAs, $Fe_3GeTe_2$, LaCl, and $EuCd_2As_2$ have been reported as well [16]. Recently, there have been several efforts to systematically identify topological materials, especially for the nonmagnetic systems

*kamal.choudhary@nist.gov

[23,24,29–31]. The SOS technique has been successfully used to identify thousands of 3D nonmagnetic insulators, SMs [23], as well as 2D nonmagnetic and magnetic insulators and SMs such as $VAg(PSe_3)_2$, $ZrFeCl_6$, MnSe, and $TiCl_3$ [24]. Identification of MTIs and MSMs has been developed by topological quantum chemistry groups [32,33] in which wave function symmetry indicators are used to identify topological materials.

In this paper, we screen for 3D MTIs and SMs using the SOS technique. We then analyze the resulting high-SOS materials using conventional Wannier tight-binding Hamiltonian (WTBH)-based techniques to calculate Chern numbers, AHCs, Berry curvatures, and Fermi surfaces, as well as local band crossings. Starting with crystal structures optimized using the OptB88vdW [34] van der Waals (vdW) functional, we first identify materials using the Perdew–Burke–Ernzerhof (PBE) [35] generalized gradient approximation (GGA) functional and then carry out strongly constrained and appropriately normed (SCAN) [36] meta-GGA functional calculations of a subset of materials. As calculating magnetic ordering for all the possible materials is very computationally expensive, for this screening work, we initialize our calculations with ferromagnetic spin polarization only. We leave systematic magnetic calculations to follow-up studies.

While our DFT-based computational screening is relatively efficient, it is still computationally expensive when applied to a set of thousands of materials. To further accelerate the identification and characterization process, we develop classification machine learning (ML) models for metals-nonmetals, magnetic-nonmagnetic and high-SOS–low-SOS materials, which acting together can screen topological materials in different classes. Specifically, we use JARVIS-ML-based classical force-field-inspired descriptors (CFIDs) [37] and gradient boosting decision tree (GBDT) for developing the ML models. CFID-based models have been successfully used for developing more than 25 highly accurate ML property prediction models [38]. Using this approach, we can first predict topological materials using ML, then confirm with SOS and Wannier tight-binding (WTB) approaches. The selected materials can be promising for experimental synthesis and characterizations. All the data and models generated through this work are publicly distributed through JARVIS-DFT [23,24,38], JARVIS-WTB [39], and JARVIS-ML Web apps [38]. We also share the computational tools and workflows developed for this paper through JARVIS-Tools open access software to enhance the reproducibility and transparency of our work. As SOS is a computational screening technique for topological materials, there are many experimental techniques to delineate topological characteristics such as ARPES, spin Hall effect (SHE), and quantum Hall effect. In this paper, we use some of these techniques to support the findings of spillage-based two-screened materials.

This paper is organized as follows: first, we show the screening strategy for high-SOS magnetic materials and present statistical analysis of some of their properties. Next, we show band structures and k-point-dependent SOS for a few example candidate materials to illustrate the strategy. After that, we further analyze selected insulating and metallic band structures with WTB approaches. Then we analyze the periodic table distribution trends and develop ML classification models to accelerate the identification processes. Finally, we show experimental characterizations of a few candidate materials.

## II. METHODS

### A. DFT

DFT calculations were carried out using the Vienna *Ab initio* simulation package (VASP) [40,41] software using the workflow [42] given on our JARVIS-Tools Github page [43]. We used the OptB88vdW functional [34], which gives accurate lattice parameters for both vdW and non-vdW (3D bulk) solids [44]. We optimized the crystal structures of the bulk and monolayer phases using VASP with OptB88vdW. The initial screening step for $<1.5$ eV band gap materials was done with OptB88vdW band gaps from the JARVIS-DFT database [45]. Because SOC is not currently implemented for OptB88vdW in VASP, we carried out spin-polarized PBE and spin-orbit PBE calculations to calculate the SOS for each material. Such an approach has been validated by Refs. [23,46]. The crystal structure was optimized until the forces on the ions were $<0.01$ eV/Å and energy $<10^{-6}$ eV. We used Wannier90 [47] and WannierTools [48] to perform the Wannier-based evaluation of topological invariants. We used WTBH calculations with high quality (MaxDiff $<0.1$ eV) [39] to predict topological invariants, surface band structures, Fermi surfaces, and AHC.

As introduced in Ref. [22], we calculated the SOS $\eta(\mathbf{k})$ given by the following equation:

$$\eta(\mathbf{k}) = n_{\text{occ}}(\mathbf{k}) - \text{Tr}(P\tilde{P}), \quad (1)$$

where $P(\mathbf{k}) = \sum_{n=1}^{n_{\text{occ}}(\mathbf{k})} |\psi_{n\mathbf{k}}\rangle\langle\psi_{n\mathbf{k}}|$ is the projector onto the occupied wave functions without SOC, and $\tilde{P}$ is the same projector with SOC for band $n$ and k-point $\mathbf{k}$. We used a $\mathbf{k}$-dependent occupancy $n_{\text{occ}}(\mathbf{k})$ of the nonspin-orbit calculation so that we could treat metals, which have varying number of occupied electrons at each k-point [23]. Here, Tr denotes trace over the occupied bands. We can write the $\eta(\mathbf{k})$ equivalently as

$$\eta(\mathbf{k}) = n_{\text{occ}}(\mathbf{k}) - \sum_{m,n=1}^{n_{\text{occ}}(\mathbf{k})} |M_{mn}(\mathbf{k})|^2, \quad (2)$$

where $M_{mn}(\mathbf{k}) = \langle\psi_{m\mathbf{k}}|\tilde{\psi}_{n\mathbf{k}}\rangle$ is the overlap between occupied Bloch functions with and without SOC at the same wave vector $\mathbf{k}$. If the SOC does not change the character of the occupied wave functions, the SOS is near zero, while band inversion results in a large SOS. After SOS calculations, we ran Wannier-based Chern and $Z_2$-index calculations for these materials.

The Chern number $C$ was calculated over the Brillouin zone as

$$C = \frac{1}{2\pi} \sum_n \int d^2\mathbf{k}\,\Omega_n, \quad (3)$$

$$\Omega_n(\mathbf{k}) = -\,\text{Im}\langle\nabla_{\mathbf{k}}u_{n\mathbf{k}}| \times |\nabla_{\mathbf{k}}u_{n\mathbf{k}}\rangle$$
$$= \sum_{m\neq n} \frac{2\text{Im}\langle\psi_{n\mathbf{k}}|\hat{v}_x|\psi_{m\mathbf{k}}\rangle\langle\psi_{m\mathbf{k}}|\hat{v}_y|\psi_{n\mathbf{k}}\rangle}{(\omega_m - \omega_n)^2}. \quad (4)$$

Here, $\Omega_n$ is the Berry curvature, $u_{n\mathbf{k}}$ being the periodic part of the Bloch wave in the $n$th band, $E_n = \hbar\omega_n$, and $v_x$ and $v_y$ are velocity operators. The Berry curvature as a function of $\mathbf{k}$ is given by

$$\Omega(\mathbf{k}) = \sum_n f_{nk}\Omega_n(\mathbf{k}). \tag{5}$$

Here, $f_{nk}$ represents the Fermi occupation for band $n$ at k-point $\mathbf{k}$. Then the intrinsic AHC $\sigma_{xy}$ in the $xy$ plane with $e$ as the electron charge and $\hbar$ as the Planck's constant for the Berry curvature $\Omega(\mathbf{k})$ (as defined above) is given by

$$\sigma_{xy} = -\frac{e^2}{\hbar} \int \frac{d^3\mathbf{k}}{(2\pi)^3} \Omega(\mathbf{k}). \tag{6}$$

In addition to searching for gapped phases, we also searched for Dirac and Weyl SMs by numerically searching for band crossings between the highest occupied and lowest unoccupied bands, using the algorithm from WannierTools [48]. This search for crossings can be performed efficiently because it takes advantage of Wannier-based band interpolation. In an ideal case, the band crossings are the only points at the Fermi level; however, in most cases, we find additional trivial metallic states at the Fermi level. The surface spectrum was calculated by using the Wannier functions and the iterative Green's function method [49–51].

Starting from ∼40 000 materials in the JARVIS-DFT database, we screened for materials with magnetic moment $>0.5\,\mu$B and having heavy elements (atomic weight $\geqslant 65$) and band gaps $<1.5$ eV. After carrying out SOS calculations on them, we broadly classified them into insulators and SMs with nonvanishing and vanishing electronic band gaps. For materials with high SOS, we ran Wannier calculations to calculate the Chern number, AHC, surface band structures, and Fermi surfaces. We also ran SCAN functional-based calculations on the high-SOS materials to check the changes in band gaps and magnetic moments. So far, we have calculated 11 483 SOSs for both magnetic-nonmagnetic and metallic-nonmetallic systems.

### B. ML model

The ML models were trained using CFIDs and supervised ML techniques using gradient boosting techniques in the LightGBM [52] package [42]. The CFID gives a unique representation of a material using structural (such as radial, angular, and dihedral distributions), chemical, and charge descriptors. The CFID provides 1557 descriptors for each material. We used VarianceThreshold and StandardScaler preprocessing techniques available in scikit-learn before applying the ML technique to remove low-variance descriptors and standardize the descriptor set. We used DFT data for developing ML models for high-low spillage (using several thresholds such as 0.1, 0.25, 0.5, 0.75, and 1.0), high-low magnetic moment (threshold 0.5 $\mu$B), and high-low band gap (threshold 0.0 eV) to further accelerate the screening process.

The CFID has been recently used to develop several high-accuracy ML models for material properties such as formation energies, band gaps, refractive index, bulk and shear modulus and exfoliation energies k-points, cutoffs, and solar-cell efficiencies. The accuracy of the model was evaluated based on

area under the curve (AUC) for the receiver operating characteristic (ROC). We used a fivefold cross-validation strategy to obtain the mean AUC as well as the standard deviation.

### C. Experimental details

#### 1. CoNb$_3$S$_6$

Single crystals of CoNb$_3$S$_6$ were grown by chemical vapor transport using iodine as the transport agent [42]. First, a polycrystalline sample was prepared by heating stoichiometric amounts of cobalt powder (Alfa Aesar 99.998%), niobium powder (Johnson Matthey Electronics 99.8%), and sulfur pieces (Alfa Aesar 99.9995%) in an evacuated silica ampoule at 900 °C for 5 d. Subsequently, 2 g of the powder was loaded together with 0.5 g of iodine in a fused silica tube of 14 mm inner diameter. The tube was evacuated and sealed under vacuum. The ampoule of 11 cm length was loaded in a horizontal tube furnace in which the temperature of the hot zone was kept at 950 °C and that of the cold zone was ≈850 °C for 7 d. Several CoNb$_3$S$_6$ crystals formed with a distinct, well-faceted flat platelike morphology. The crystals of CoNb$_3$S$_6$ were examined by single crystal x-ray diffraction at room temperature. Compositional analysis was done using energy dispersive x-ray spectroscopy (EDS) at the Electron Microscopy Center, ANL.

Transport measurements were performed on a Quantum Design Physical Property Measurement System following a conventional 4-probe method. Au wires of 25 $\mu$m diameter were attached to the sample with Epotek H20E silver epoxy. An electric current of 1 mA was used for the transport measurements. The following method was adopted for the contact misalignment correction in Hall effect measurements. The Hall resistance was measured at $H = 0$ by decreasing the field from the positive magnetic field (RH+), where $H$ represents the external magnetic field. Again, the Hall resistance was measured at $H = 0$ by increasing the field from negative magnetic field (RH−). The average of the absolute value of (RH+) and (RH−) was then subtracted from the measured Hall resistance. The conventional antisymmetrization method was also used for the Hall resistance measured at 28 K (above TN) and at 2 K [where no anomalous Hall effect (AHE) was observed], which gave the same result as obtained from the former method.

#### 2. Mn$_3$Ge

In inverse SHE (ISHE), a pure spin current $\vec{J}_S$ gets converted to a charge current $\vec{J}_C$ due to spin-dependent asymmetric scattering phenomena [42]. To maximize the ISHE signal, the external magnetic field was applied along [1$\bar{1}$00], and direct current (dc) voltage was measured along [11$\bar{2}$0] directions. An optical image of the spin-pumping (SP) device is shown in Fig. 6(b). For SP-FMR measurements, (i) Mn$_3$Ge (100 nm)/Py (10 nm), (ii) Pt (10 nm)/Py (10 nm), and (iii) Py (10 nm) samples were prepared on sapphire substrate. They were fabricated into 1000 $\mu$m × 200 $\mu$m bars by photolithography and ion milling. Coplanar waveguides (CPWs) with 170-nm-thick Ti (20 nm)/Au (150 nm) were subsequently fabricated. Using the inductively coupled plasma chemical vapor deposition method, an additional SiN (150 nm) layer
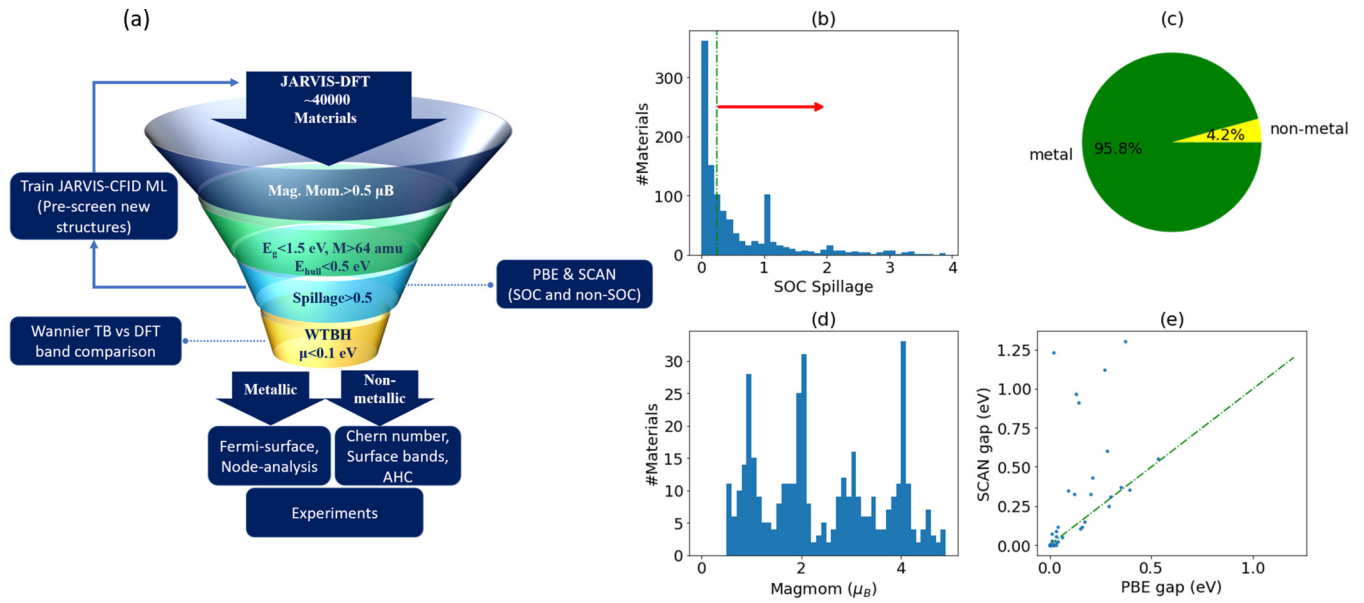
FIG. 1. Flow chart for screening high-spillage materials and analysis. (a) Flowchart for screening, (b) spillage distribution analysis for all the materials under investigation, (c) pie chart showing high-spillage insulators and metals, (d) magnetic moment distribution for high-spillage materials, (e) PBE vs SCAN band gaps.

was deposited between CPW and the sample for electric isolation. The microwave frequencies were tuned between 10 and 18 GHz with varying power (12–18 dBm), while magnetic field was swept between −0.4 and 0.4 T along the CPW axis. Measurements were performed at room temperature, and field resolution of 2 mT was adopted throughout.

## III. RESULTS AND DISCUSSION

A flow chart for screening magnetic topological materials is shown in Fig. 1(a). First, we screened for materials with net magnetic moment ($> 0.5\,\mu B$) in the ferromagnetic phase, which led to 8651 candidates out of 39 315 materials in the JARVIS-DFT database. Then we looked for materials that were reasonably stable and likely to display topological band inversion by screening for materials that (a) were $< 0.5\,\mathrm{eV}$/atom above the convex hull, (b) had small non-SOC band gaps ($< 1.5\,\mathrm{eV}$), and (c) had at least 1 atom with high atomic mass ($M > 64$). This resulted in 4734 remaining materials. We have computed the SOS with PBE + SOC for 1745 materials (prioritizing the calculations of the number of atoms in a unit cell $< 20$). Next, we performed WTBH calculations with high quality (MaxDiff $< 0.1\,\mathrm{eV}$) [39] to predict topological invariants, surface band structures, Fermi surfaces, and AHC. So far, we have obtained high-quality WTBHs for 146 candidate materials. To study the effects of exchange correlation, we ran SCAN [36] meta-GGA functional calculations for high-SOS materials (Table S1, see the Supplemental Material [53]). Note that it may be difficult to carry out high dense k-point DFT calculations with SOC for thousands of materials, so after the WTBH generation, we carried out high-density k-point calculation WTB models to find if the band gap truly existed. Most of the materials studied in this paper come from experimentally determined structures from the inorganic crystal structure database (ICSD) [54].

In Fig. 1(b), we show the SOS distribution of the materials investigated in this paper. As the SOS can be related to the number of band-inverted electrons at a k-point, we observe spikes at integer numbers [22–24]. SOC can also change the mixing between different orbitals, rather than pure band inversion, which results in fractional values. As shown in Fig. 1(b), using a threshold of 0.25 for screening eliminates 51% of materials, leaving 25 insulating and 564 metallic candidate materials with high SOS and nonzero magnetic moment. Similarly, in our previous papers for 3D nonmagnetic and 2D materials [22–24], the SOS technique was shown to discard more than 50% candidates in the initial screening steps. A material with nonzero SOS is a candidate topological material, and we choose a threshold of 0.25 to narrow down the options. Any nonzero value of the SOS is a sign of changes in the band structure due to SOC, but for noninsulators, there is no specific value that can guarantee or exclude specific topological features in the band structure. We set the threshold pragmatically to attempt to balance the number of false positives vs false negatives and to select a reasonable number of promising materials to subject to more computationally expensive screening. We also provide all of the spillage data in the Supplemental Material (Table S2 [53]) so that users can make their own judgment as to which materials are worth studying in more detail, given their interests and constraints. In Fig. 1(c), we show the pie chart for high-SOS insulating and metallic material distribution. This suggests that MTIs are far rarer than SMs. In the later sections, we discuss with examples some of the insulating and metallic high-SOS materials and characterize them using the WTBH approach also. Next, in Fig. 1(d), we observe that the magnetic moment of the systems could be up to $6\,\mu B$ with mostly integer or close to integer values for the magnetic moments. Due to the large computational expense of searching for magnetic ground states, we only considered ferromagnetic spin configuration, i.e., all spins of the system in a fixed direction. We expect that many of the

high-SOS materials that we find to be ferromagnetic may turn out to have lower energies in the antiferromagnetic or ferrimagnetic configurations. In Fig. 1(e), we compare the band gaps of the materials with PBE + SOC and SCAN + SOC for 65 high-SOS materials. Recently, the SCAN functional has been proposed as the functional to solve the band gap and high correlated system issues which can be important for magnetic topological materials. SCAN has been shown to predict band gaps and magnetic moments better than the local density approximation (LDA), LDA + U, and PBE in many cases [55–57]. We observe that SCAN + SOC bands are very close or in some cases slightly higher than PBE + SOC band gaps for most of the materials. However, for some systems, there can be a large difference such as for $MnSb_4O_2$ (JVASP-44705). Some of the materials that are metallic in PBE turn into insulating in SCAN predictions [for example, $LiMnAsO_4$ (JVASP-55805) and $Li_4Fe_3CoO_8$ (JVASP-42538)], which indicates that magnetic metals found to be high SOS using PBE may in fact be small gap TIs. We provide more detailed PBE vs SCAN comparisons in the Supplemental Material (Table S1 [53]).

In Fig. 2, we show the nonspin-orbit and spin-orbit band structures for a few screened insulating and semimetallic systems along with corresponding SOS plots such as (a) $Mn_2Sb$ (JVASP-15693), (b) $NaMnTe_2$ (JVASP-16806), (c) $Rb_3Ga$ (JVASP-38248), (d) CoSI (JVASP-78508), (i) $Mn_3Sn$ (JVASP-18209), (j) $Sc_3In$ (JVASP-17478), (k) $Sr_3Cr$ (JVASP-37600), (l) $Mn_3Ge$ (JVASP-78840), (q) $NaRuO_2$ (JVASP-8122), (r) $CoNb_3S_6$ (JVASP-21459), (s) $Y_3Sn$ (JVASP-37701), (t) $CaMnBi_2$ (JVASP-18532). A summary of the above materials is also provided in Table I.

The red and blue lines show SOC and non-SOC band structures, respectively. The k-dependent spillage is shown in (e), (f), (g), (h), (m), (n), (o), (p), (u), (v), (w), and (x). Such band structures and spillage plots for 11 483 materials (including 2D and 3D magnetic and nonmagnetic systems) are distributed through the JARVIS-DFT Web site along with several other material properties such as crystal structure, heat of formation, elastic, piezoelectric, dielectric, and thermoelectric constants. In all the cases, the spillage is >0.25, and the magnetic moments in the ferromagnetic configuration for these systems are >1 $\mu$B. The $NaRuO_2$ shows a PBE + SOC gap of 56 meV, while other materials are metallic. We note that, in some cases, the magnetic ordering or magnetic moment can change significantly when adding SOC to a calculation, resulting in a high spillage value without any direct relation to band inversion. Hence, it is important to further analyze the candidate materials by directly computing topological behavior, and we show examples of this analysis for $NaRuO_2$ and $Y_3Sn$ below.

In our earlier paper [39], we created a database of automatically generated WTBH, which we use here to analyze topological behavior and support our findings from the spillage-based screening. The accuracy of the WTBH is evaluated based on the MaxDiff criteria [39] which compares the maximum band-energy difference between DFT and WTB on k-points within and beyond our DFT calculation k-points. We set a MaxDiff (maximum energy difference at all k-points between Wannier and DFT bands) value of 0.1 eV as the tolerance for a good-quality WTBH. Out of all the spillage-based

candidate materials, we observed at least 146 of them have low MaxDiff. For the systems with high spillage and high-quality WTBH, we predict Wannier charge centers (WCCs), surface band structures, and AHC for the insulating cases and AHC, Fermi surfaces, and node plots for the metallic cases. Our Wannier database is available at Ref. [58] with interactive features. We provide heat of formation, space group, convex hull, and other important details for each material in the corresponding Web page (such as Ref. [59]) as well as in the Supplemental Material (Table S2 [53]). These Web pages can also be downloaded as extensible markup language documents containing raw data for replotting or analysis by the users.

We identify $NaRuO_2$ as a candidate 3D Chern insulator through the above systematic screening process based on PBE + SOC and SCAN + SOC. $NaRuO_2$ is a trigonal system, belonging to $R\bar{3}m$ space group. The heat of formation of the system is negative ($-1.293$ eV/atom), suggesting the system should be thermodynamically favorable. Also, the system has a formation energy that is 0.089 eV/atom above the convex hull, suggesting that the system is slightly unstable but in a range where is may be synthesizable, and it has in fact been synthesized experimentally [60]. We observe that this material is metallic without SOC [Fig. 2(a)], but as we turn on SOC, a gap opens at the B and X points, which results in high spillage of 0.56. At least 18 materials show band gap opening due to inclusion of SOC. Next, we calculate the Chern number using the WCCs, as shown in Figs. 3(a) and 3(b). We observe gapless charge centers, indicating that the material is a 3D Chern insulator. The Chern number of four planes, i.e., $k_1 = 0.0$; $k_1 = 0.5$; $k_2 = 0.0$; $k_2 = 0.5$ ($k_3 = 0.0$; $k_3 = 0.5$ and $k_2 = 0.0$; $k_2 = 0.5$ remaining the same); where $k_1$, $k_2$, and $k_3$ in fractional units are determined as $-2$. In Fig. 3(c), we see a conducting channel in the (001) surface, suggesting that the material is conducting at its surface, but the bulk is insulating even though the time reversal is broken in the system. The Chern number is directly proportional to the AHC, which is an experimentally measured quantity. For a 3D Chern material, AHC is calculated as $\frac{C_3 b_3 e^2}{2\pi h}$ ($b_3$ is the normal lattice vector), which turns out to be 1540 ohm$^{-1}$cm$^{-1}$, which is what we find using the Wannier calculation-based quantity in Fig. 3(d). In this case, the AHC in Fig. 3(d) is quantized, which can be leveraged for precise quantum control from the perspective of building devices. In addition, we analyzed this material using SCAN + SOC, and we found that the band structure is very similar to the PBE + SOC result, and the topological properties are the same (see the Supplemental Material [53] Fig. S1).

In Fig. 4, we show the analysis of an example candidate topological metal $Y_3Sn$. $Y_3Sn$ crystallizes in the $P6_3mmc$ space group and hexagonal system, has negative formation energy ($-0.43$ eV/atom) and 0.1 eV/atom energy above the convex hull, suggesting that it should be experimentally synthesizable. The band structures in Fig. 1 show multiple band crossings for this system and have a spillage of 0.25. We plot the Fermi surface of this system in Fig. 4(a), which shows several conducting Fermi channels represented by deep blue spots. The lighter colors indicate that there are not bands at the Fermi level. This material belongs to the Kagome lattice, and such Fermi surfaces have recently gained interest due to
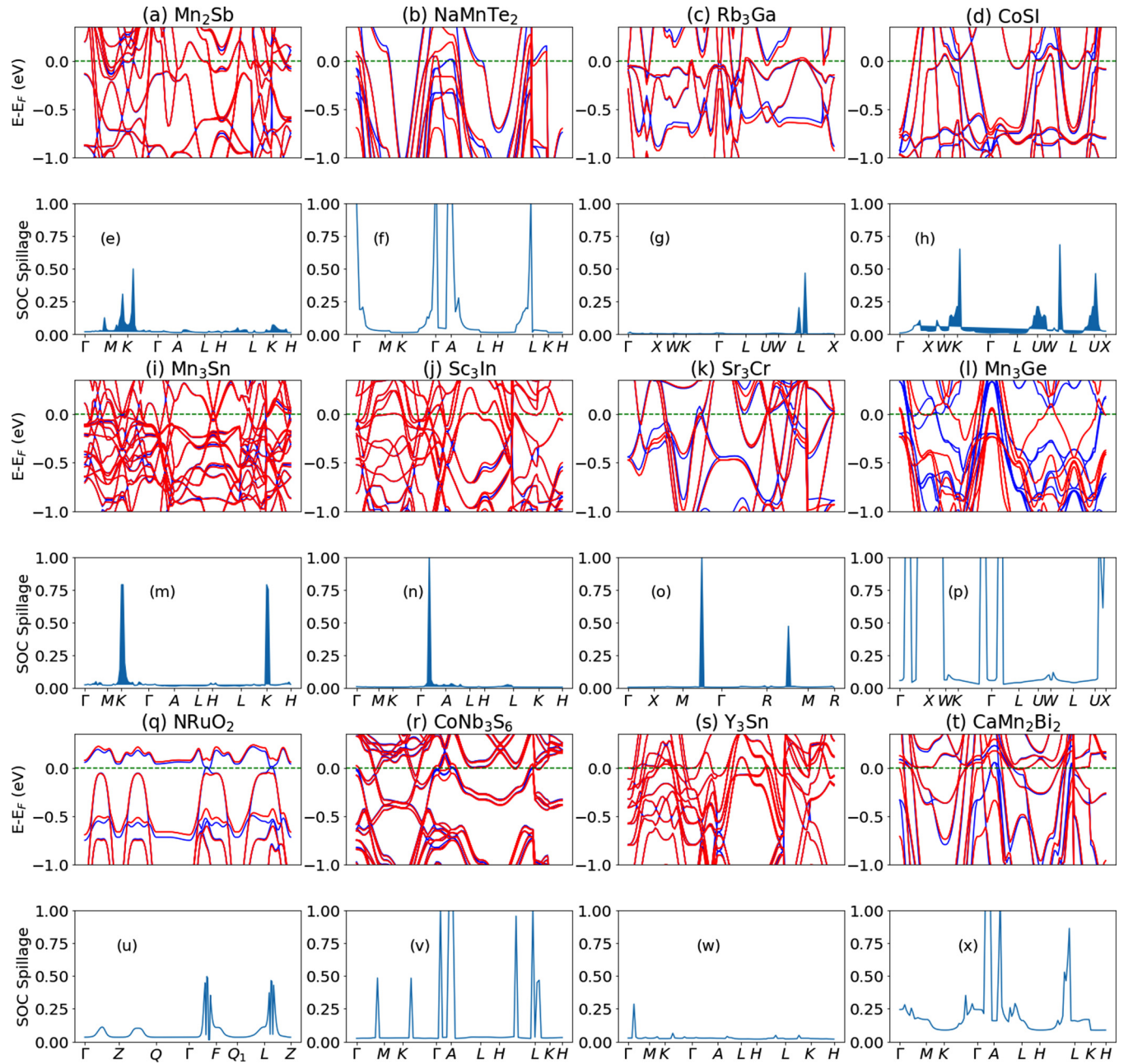
FIG. 2. Examples of band structure and k-dependent spin-orbit spillage plots for a few selected candidate materials with PBE + SOC. Band structures are shown in (a) $Mn_2Sb$ (JVASP-15693), (b) $NaMnTe_2$ (JVASP-16806), (c) $Rb_3Ga$ (JVASP-38248), (d) CoSI (JVASP-78508), (i) $Mn_3Sn$ (JVASP-18209), (j) $Sc_3In$ (JVASP-17478), (k) $Sr_3Cr$ (JVASP-37600), (l) $Mn_3Ge$ (JVASP-78840), (q) $NaRuO_2$ (JVASP-8122), (r) $CoNb_3S_6$ (JVASP-21459), (s) $Y_3Sn$ (JVASP-37701), (t) $CaMn_2Bi_2$ (JVASP-18532). The red and blue lines show SOC and non-SOC band structures, respectively. The k-dependent spillage is shown in (e), (f), (g), (h), (m), (n), (o), (p), (u), (v), (w), and (x) respectively.

unique nodal linelike features [61,62]. The (001) surface for this material also shows multiple bands crossing the Fermi level, which is shown in Fig. 4(c). We observe several nodes in this material, as shown in Fig. 4(c) with color coded energy level values. Energy levels with null value or blue color represent bands at the Fermi level. The calculated AHC of this system is shown in Fig. 4(d). The AHC is not quantized such as $NaRuO_2$, but still has a nonzero value at zero field, which can be due to the topological features of the band structure. The SCAN + SOC and PBE + SOC band structure comparison for this system is also shown in the Supplemental Material

[53] (Fig. S2), which shows shifts in energy for several bands.

As mentioned in the introduction, a symmetry indicator method [32] has also recently been used to identify magnetic topological materials. We identify the common materials between our selected candidates and those from Ref. [32]. We list the common materials in Table II. We provide chemical formula, space group, JARVIS-ID, ICSD ID, Bilbao Crystallographic Server Magnetic database (BCSMD) ID, and spillage values. We note that, in Ref. [32], they are considering materials with experimentally characterized magnetic

TABLE I. Summary of materials and their maximum spillage values as shown in Fig. 2.

| Formula | Space group | JARVIS-ID | Spillage |
|---------|-------------|-----------|----------|
| $Mn_2Sb$ | $P6_3/mmc$ | JVASP-15693 | 0.50 |
| $NaMnTe_2$ | $P\bar{3}m1$ | JVASP-16806 | 1.04 |
| $Rb_3Ga$ | $Fm\bar{3}m$ | JVASP-38248 | 0.47 |
| $CoSI$ | $F\bar{4}3m$ | JVASP-78508 | 0.69 |
| $Mn_3Sn$ | $P6_3/mmc$ | JVASP-18209 | 0.79 |
| $Sc_3In$ | $P6_3/mmc$ | JVASP-17478 | 1.01 |
| $Sr_3Cr$ | $Pm\bar{3}m$ | JVASP-37600 | 1.01 |
| $Mn_3Ge$ | $Fm\bar{3}m$ | JVASP-78840 | 3.01 |
| $NaRuO_2$ | $R\bar{3}m$ | JVASP-8122 | 0.50 |
| $CoNb_3S_6$ | $P6_322$ | JVASP-21459 | 1.03 |
| $Y_3Sn$ | $P6_3/mmc$ | JVASP-37701 | 0.29 |
| $CaMn_2Bi_2$ | $P\bar{3}m1$ | JVASP-18532 | 1.17 |

structures only, while we consider only ferromagnetic spin ordering. Despite these differences, we still find these materials to have high spillage values. Also, it is important to note that the number of well-characterized magnetic materials is small; hence, our workflow has a wider applicability.

Next, in Fig. 5, we show the likelihood that a compound containing a given element has a high spillage for the 4734 materials screened from step (a). More specifically, for every compound containing a given element, we calculate the percentage that have a spillage >0.25. Consistent with known TMs, we observe that materials containing the elements such as Mn, Re, Fe, Ir, Pt, Bi, and Pb are by far the likeliest ones to have high spillage. To contribute to SOC-induced band inversion, an element must both have significant SOC and contribute to bands located near the Fermi level, which favors heavy elements with moderate electronegativity. We use similar analysis for materials for thermoelectrics, solar
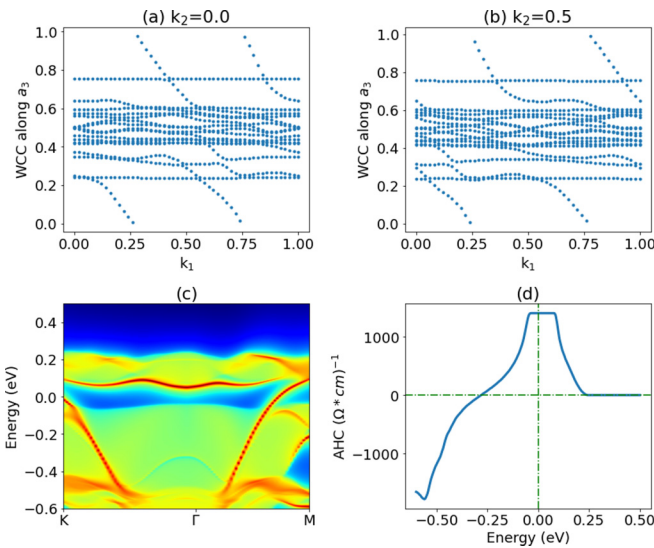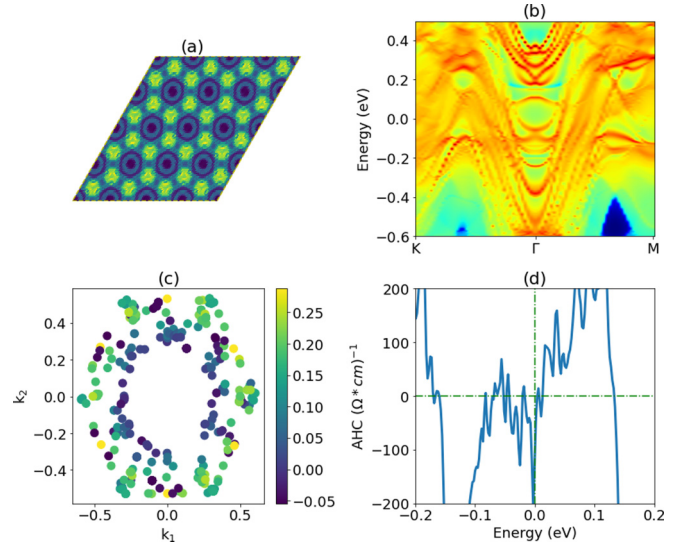


FIG. 4. Analysis for $Y_3Sn$ (JVASP-37701) as a candidate semimetal with PBE + SOC. (a) Fermi surface, (b) (001) surface band structure, (c) nodal points-lines, (d) anomalous Hall conductivity.

cells, elastic constants, etc. We can see some basic trends in the data, but we intend to move toward more ML prediction. To further accelerate the screening of magnetic topological materials, we train three classification models using CFIDs [37] to predict the spillage, magnetic moment, and band gaps, based on data from the JARVIS-DFT database. The CFIDs provide a complete set of structural chemical features (1557 for each material) which we use with the GBDT algorithm as implemented in LightGBM [52] to train high-accuracy ML models. The accuracy of the classification can be measured in terms of ROC AUC, which is 0.81 for spillage and 0.97 for both the magnetic and band gap models (using a fivefold cross-validation strategy). The ROC AUC is 0.5 for a random model and 1.0 for a perfect model. The models trained for this paper have ROC AUC > 0.81, signifying useful predictive power. We also train the spillage classification models for several threshold values: 0.1, 0.25, 0.5, 0.75, and 1 to check the influence of threshold on model performance, as shown in Fig. 6. We find that, as we increase the threshold, the ROC AUC decreases from 0.87 to 0.78, which implies while using the model for classifying high vs low spillage values, lower spillage threshold gives higher ROC AUC. Due to the fivefold cross-validation strategy, we also obtained standard deviations for all the models. The standard deviations for all the models are very small, ranging between 0.00 and 0.01, suggesting shuffling of data during training and testing has minimal effect on the performance. The gradient boosting algorithm allows for feature importance to be extracted after training the model. Some of the high-importance descriptors of the ML models are unfilled $d$ orbitals and electronegativity, which is intuitively reasonable. After training the ML models, we applied them on 1 399 770 materials from JARVIS, AFLOW [63], Materials Project [42], and Open Quantum Materials Database [64] to find 77 210 likely high-SOS materials. The ML-screened materials can then be subjected to the DFT workflow used in this paper [see Fig. 1(a)] to further



FIG. 3. Wannier charge center (WCC), surface band structure and anomalous Hall conductivity for $NaRuO_2$ (JVASP-8122) with PBE + SOC. (a) and (b) WCCs along the third lattice vector ($a_3$) for (a) $k_2 = 0.0$, and (b) for $k_2 = 0.5$, (c) (001) surface band structure, (d) AHC ($\sigma_{xy}$) plot for the compound.

TABLE II. Common materials identified from SOC-spillage and symmetry indicator method [32].

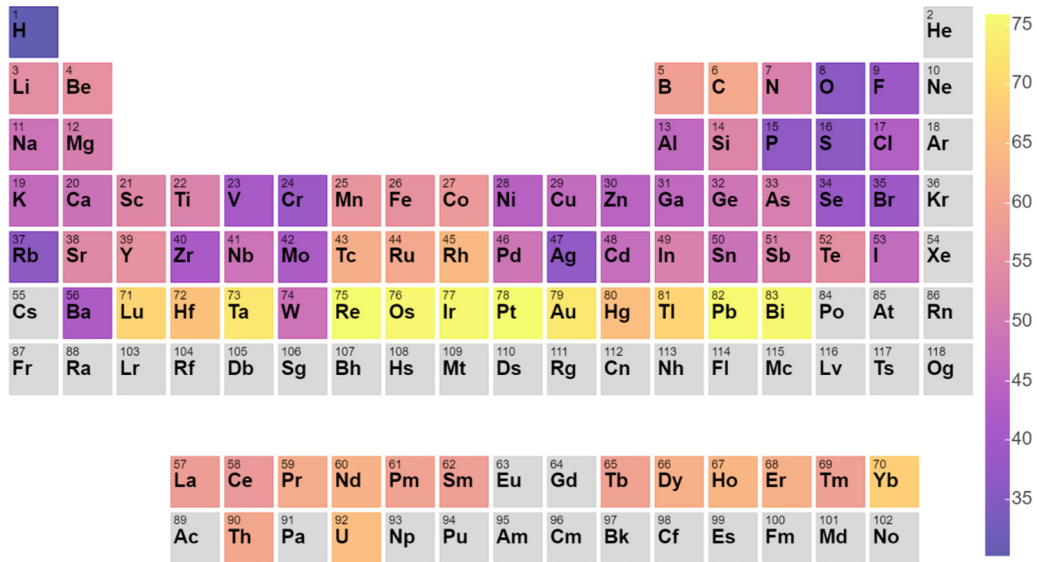| Formula | Space group | JARVIS-ID | ICSD-ID | BCSMD-ID | Spillage |
|---|---|---|---|---|---|
| $Mn_3GaC$ | $Pm\bar{3}m$ | JVASP-18041 | 23586 | 1.153 | 0.10 |
| $Mn_3ZnC$ | $Pm\bar{3}m$ | JVASP-15104 | 618284 | 2.19 | 0.60 |
| $Mn_3GaN$ | $Pm\bar{3}m$ | JVASP-51043 | 87399 | 0.177 | 0.20 |
| $Fe_2As$ | $P4/nmm$ | JVASP-17705 | 42335 | 1.131 | 0.10 |
| $Mn_3Sn$ | $P6_3/mmc$ | JVASP-18209 | 643730 | 0.199 | 0.80 |
| $Sr_2Mn_3(AsO)_2$ | $I4/mmm$ | JVASP-17462 | 81803 | 0.212 | 3.37 |
| $Sr_2IrO_4$ | $I4_1/acd$ | JVASP-21528 | 78261 | 1.3 | 2.28 |



FIG. 5. Periodic table trends. Periodic table trends of compounds with high-spillage values. The elements in a material are weighed 1 or 0 if the material has high or low values. Then the percentage probability of finding the element in a high-value material is calculated.
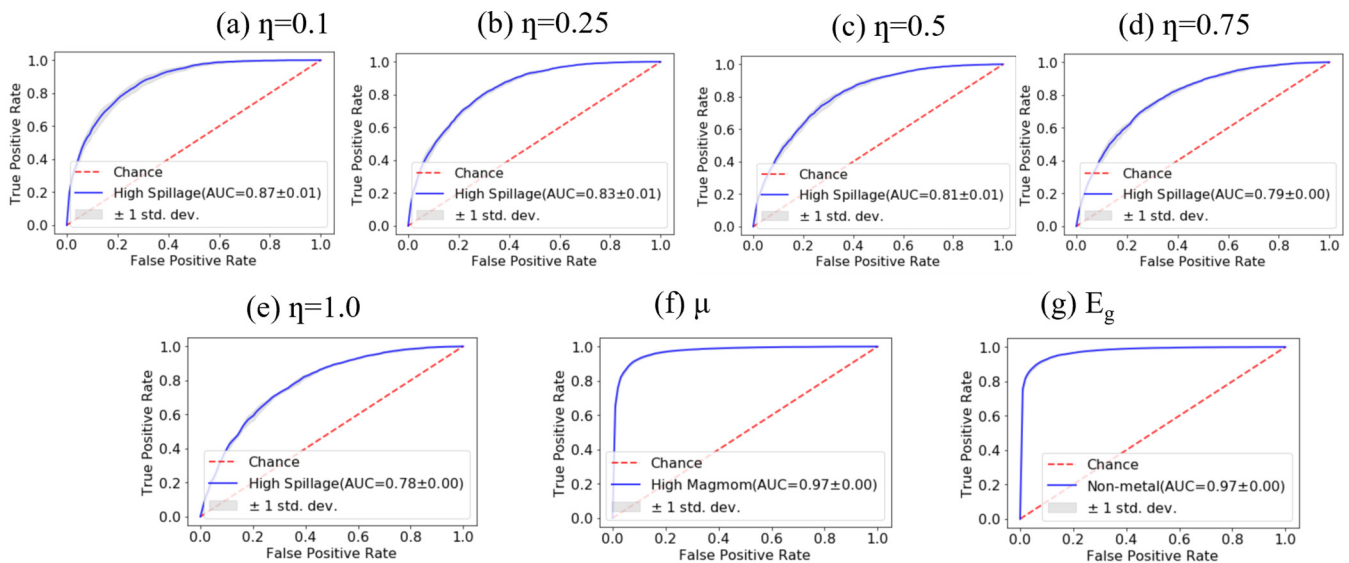


FIG. 6. Classification model receiver operating characteristic (ROC) curves. (a) High-low spillage model, threshold 0.1, (b) spillage model, threshold 0.25, (c) spillage model, threshold 0.5, (d) spillage model, threshold 0.75, (e) spillage model, threshold 1.0, (f) high-low magnetic moment, threshold 0.5 $\mu$B, (g) metals-nonmetals based on electronic band gaps, threshold 0.05 eV. All models are evaluated using fivefold cross-validation strategy, and corresponding standard deviation is reported in each plot.
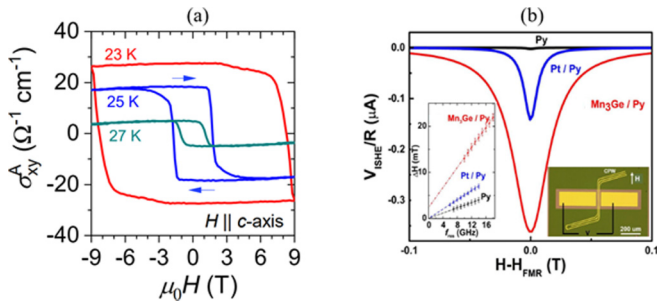
FIG. 7. Experimental measurements of some of the candidate materials. (a) Anomalous Hall effect of $CoNb_3S_6$, (b) comparison of inverse spin-Hall signal (symmetric component) among measured devices for $Mn_3Ge$. Right inset: Optical image of the spin-pumping ferromagnetic resonance (SP-FMR) device. Left inset: Linear fit to the resonance linewidth ($\Delta H$) at various resonance frequencies.

accelerate the search for magnetic topological materials. The ML models are distributed through the JARVIS-ML Web app.

Next, we discuss experimental results that support some of our theoretical findings. The AHE was first observed in ferromagnets where its origin lies in the interplay between SOC and magnetization. Berry phase calculations have been proven accurate to predict SOC-induced intrinsic AHE in ferromagnets, including Weyl (semi)metals, noncollinear antiferromagnets, noncoplanar magnets, and other nontrivial spin textures [1,2]. We focus on two compounds: $CoNb_3S_6$ and $Mn_3Ge$. In Fig. 7(a), we show the experimental AHC as a function of magnetic field at 23, 25, and 27 K for $CoNb_3S_6$. $CoNb_3S_6$ shows an AHE below the Néel temperature of 27.5 K [17], whereby the AHC attains the value $27\,\Omega^{-1}\,cm^{-1}$ at 23 K. Furthermore, Hall conductivity measured on thinned down samples shows an enhancement in the AHC that reaches about 60% of the quantized value of $(e^2/h)$ [65]. The collinear antiferromagnetic structure determined by neutron diffraction experiment [66] does not explain this large AHE in $CoNb_3S_6$, indicating that the AHE is intrinsic to the electronic structure in the magnetic state. Corresponding computational non-SOC and SOC band structures for this system, which has a maximum spillage value of 1.03, indicating the topological nature of the electronic band structure, are shown in Fig. 2(r).

In Fig. 7(b), we show the SP-FMR measurements by utilizing the ISHE for $Mn_3Ge$. Several previous studies have suggested the topologically nontrivial nature of $Mn_3Ge$ [67–69]. In ISHE, a pure spin current $\vec{J}_S$ gets converted

to a charge current $\vec{J}_C$ due to spin-dependent asymmetric scattering phenomena. For SP-FMR measurements, $Mn_3Ge$ (100 nm)/Permalloy (Py) (10 nm), Pt (10 nm)/Py (10 nm), and Py (10 nm) samples were prepared on sapphire substrate. A Pt device was also fabricated and analyzed because it provides an ideal benchmark for ISHE comparison. Figure 7(b) shows the comparison between the ISHE charge current ($V_{ISHE}/R_{eq}$) for all three devices, where $R_{eq}$ is the total device resistance across the contact pads. Resistance values $R_{eq}$ for all devices were measured at room temperature in four-probe configuration. As expected, the Py single-layer device is unaffected by ISHE, and thus, $V_{sp}$ (total dc voltage due to SP) is entirely antisymmetric. On the other hand, the peak $V_{ISHE}/R_{eq}$ value of the $Mn_3Ge$/Py device is significantly larger than that of the Pt/Py device. The ratio of spin Hall angles $\theta_{SH}^{Mn3Ge}/\theta_{SH}^{Pt}$ is estimated to be around $8 \pm 2$. The larger spin Hall angle of $Mn_3Ge$ is a result of nontrivial band topology which is consistent with the spillage signature.

## IV. CONCLUSIONS

We have demonstrated the applicability of SOS, ML, and experimental techniques to identify and characterize magnetic topological materials. We have also shown basic trends in the topological chemistry with statistical analysis and periodic table distribution plots. Because we employ a high-throughput approach to screen a large database, we employ several assumptions, including assuming a ferromagnetic spin ordering and not performing detailed analysis of the dynamic or thermodynamic stability of our candidate materials. Detailed investigation of each material is out of the scope of this paper and will be undertaken in future work. We have made our datasets and tools publicly available to enhance the reproducibility and transparency of our work. We believe that our work can be of great help to guide future computational or experimental efforts to discover and characterize new magnetic topological materials.

[1] F. Ortmann, S. Roche, and S. O. Valenzuela, *Topological insulators: Fundamentals and perspectives* (Wiley-VCH, New York, 2015).

[2] D. Vanderbilt, *Berry Phases in Electronic Structure Theory: Electric Polarization, Orbital Magnetization and Topological Insulators* (Cambridge University Press, Cambridge, 2018).

[3] M. Z. Hasan and C. L. Kane, Colloquium: Topological insulators, Rev. Mod. Phys. **82**, 3045 (2010).

[4] K. S. Novoselov, A. K. Geim, S. Morozov, D. Jiang, M. Katsnelson, I. Grigorieva, S. Dubonos, and A. A. Firsov, Two-dimensional gas of massless Dirac fermions in graphene, Nature **438**, 197 (2005).

[5] S.-M. Huang, S.-Y. Xu, I. Belopolski, C.-C. Lee, G. Chang, B. Wang, N. Alidoust, G. Bian, M. Neupane, and C. Zhang, A Weyl fermion semimetal with surface Fermi arcs in the transition metal monopnictide TaAs class, Nat. Comm. **6**, 7373 (2015).

[6] L. Fu, Topological Crystalline Insulators, Phys. Rev. Lett. **106**, 106802 (2011).

[7] G. Bian, T.-R. Chang, R. Sankar, S.-Y. Xu, H. Zheng, T. Neupert, C.-K. Chiu, S.-M. Huang, G. Chang, and I. Belopolski, Topological nodal-line fermions in spin-orbit metal PbTaSe$_2$, Nat. Comm. **7**, 10556 (2016).

[8] A. Burkov, M. Hook, and L. Balents, Topological nodal semimetals, Phys. Rev. B **84**, 235126 (2011).

[9] N. Varnava and D. Vanderbilt, Surfaces of axion insulators, Phys. Rev. B **98**, 245117 (2018).

[10] S. Raghu, X.-L. Qi, C. Honerkamp, and S.-C. Zhang Topological Mott Insulators, Phys. Rev. Lett. **100**, 156401 (2008).

[11] F. Schindler, A. M. Cook, M. G. Vergniory, Z. Wang, S. S. Parkin, B. A. Bernevig, and T. Neupert, Higher-order topological insulators, Sci. Adv. **4**, eaat0346 (2018).

[12] Y. Zhou and K. Kanoda, Quantum spin liquid states, J. Rev. Mod. Phys. **89**, 025003 (2017).

[13] K. Sun, H. Yao, E. Fradkin, and S. Kivelson, Topological Insulators and Nematic Phases from Spontaneous Symmetry Breaking in 2D Fermi Systems with a Quadratic Band Crossing, Phys. Rev. Lett. **103**, 046811 (2009).

[14] T. Thonhauser and D. Vanderbilt, Insulator/Chern-insulator transition in the Haldane model, Phys. Rev. B **74**, 235111 (2006).

[15] Y. Tokura, K. Yasuda, and A. Tsukazaki, Magnetic topological insulators, Nat. Rev. Phys. **1**, 126 (2019).

[16] J. Zou, Z. He, and G. Xu, The study of magnetic topological semimetals by first principles calculations, npj Comput. Mater. **5**, 96 (2019).

[17] N. J. Ghimire, A. Botana, J. Jiang, J. Zhang, Y.-S. Chen, and J. Mitchell, Large anomalous Hall effect in the chiral-lattice antiferromagnet CoNb$_3$S$_6$, Nat. Commun. **9**, 1 (2018).

[18] D. Hong, N. Anand, C. Liu, H. Liu, I. Arslan, J. E. Pearson, A. Bhattacharya, and J. Jiang, Large anomalous Nernst and inverse spin-Hall effects in epitaxial thin films of Kagome semimetal Mn$_3$Ge, Phys. Rev. Mater. **4**, 094201 (2020).

[19] L. Liu, T. Moriyama, D. Ralph, and R. Buhrman, Spin-Torque Ferromagnetic Resonance Induced by the Spin Hall Effect, Phys. Rev. Lett. **106**, 036601 (2011).

[20] B. Lv, T. Qian, and H. Ding, Angle-resolved photoemission spectroscopy and its application to topological materials, Nat. Rev. Phys. **1**, 609 (2019).

[21] L. Simon, C. Bena, F. Vonau, M. Cranney, and D. Aubel, Fourier-transform scanning tunnelling spectroscopy: The possibility to obtain constant-energy maps and band dispersion using a local measurement, J. Phys. D **44**, 464010 (2011).

[22] J. Liu and D. Vanderbilt, Spin-orbit spillage as a measure of band inversion in insulators, Phys. Rev. B **90**, 125133 (2014).

[23] K. Choudhary, K. F. Garrity, and F. Tavazza, High-throughput discovery of topologically non-trivial materials using spin-orbit spillage, Sci. Rep. **9**, 8534 (2019).

[24] K. Choudhary, K. F. Garrity, J. Jiang, R. Pachter, and F. Tavazza, Computational search for magnetic and non-magnetic 2D topological materials using unified spin-orbit spillage screening, npj Comput. Mater. **6**, 1 (2020).

[25] M. M. Otrokov, I. I. Klimovskikh, H. Bentmann, D. Estyunin, A. Zeugner, Z. S. Aliev, S. Gaß, A. Wolter, A. Koroleva, and A.

M. Shikin, Prediction and observation of an antiferromagnetic topological insulator, Nature **576**, 416 (2019).

[26] J. Li, Y. Li, S. Du, Z. Wang, B.-L. Gu, S.-C. Zhang, K. He, W. Duan, and Y. Xu, Intrinsic magnetic topological insulators in van der Waals layered MnBi$_2$Te$_4$-family materials, Sci. Adv. **5**, eaaw5685 (2019).

[27] S. Chowdhury, K. F. Garrity, and F. Tavazza, Prediction of Weyl semimetal and antiferromagnetic topological insulator phases in Bi$_2$MnSe$_4$, npj Comput. Mater. **5**, 33 (2019).

[28] T. Zhu, A. J. Bishop, T. Zhou, M. Zhu, D. J. O'Hara, A. A. Baker, S. Cheng, R. C. Walko, J. J. Repicky, and J. A. Gupta, Magnetic properties and electronic structure of magnetic topological insulator MnBi$_2$Se$_4$, arXiv:2003.07938 (2020).

[29] M. Vergniory, L. Elcoro, C. Felser, N. Regnault, B. A. Bernevig, and Z. J. N. Wang, A complete catalogue of high-quality topological materials, Nature **566**, 480 (2019).

[30] T. F. Tang, H. C. Po, A. Vishwanath, and X. Wan, Comprehensive search for topological materials using symmetry indicators, Nature **566**, 486 (2019).

[31] B. Bradlyn, L. Elcoro, J. Cano, M. Vergniory, Z. Wang, C. Felser, M. Aroyo, and B. A. Bernevig, Topological quantum chemistry, Nature **547**, 298 (2017).

[32] Y. Xu, L. Elcoro, Z.-D. Song, B. J. Wieder, M. Vergniory, N. Regnault, Y. Chen, C. Felser, and B. A. Bernevig, High-throughput calculations of magnetic topological materials, Nature **586**, 702 (2020).

[33] N. C. Frey, M. K. Horton, J. M. Munro, S. M. Griffin, K. A. Persson, and V. B. Shenoy, High-throughput search for magnetic and topological order in transition metal oxides, Sci. Adv. **6**, eabd1076 (2020).

[34] J. Klimeš, D. R. Bowler, and A. Michaelides, Chemical accuracy for the van der Waals density functional, J. Phys. Cond. Mat. **22**, 022201 (2009).

[35] J. P. Perdew, K. Burke, and M. Ernzerhof, Generalized Gradient Approximation Made Simple, Phys. Rev. Lett. **77**, 3865 (1996).

[36] J. Sun, A. Ruzsinszky, and J. P. Perdew, Strongly Constrained and Appropriately Normed Semilocal Density Functional, Phys. Rev. Lett. **115**, 036402 (2015).

[37] K. Choudhary, B. DeCost, and F. Tavazza, Machine learning with force-field-inspired descriptors for materials: fast screening and mapping energy landscape, Phys. Rev. Mater. **2**, 083801 (2018).

[38] K. Choudhary, K. F. Garrity, A. C. Reid, B. DeCost, A. J. Biacchi, A. R. H. Walker, Z. Trautt, J. Hattrick-Simpers, A. G. Kusne, and A. Centrone, The joint automated repository for various integrated simulations (JARVIS) for data-driven materials design, npj Comput. Mater. **6**, 1 (2020).

[39] K. F. Garrity and K. Choudhary, Database of Wannier tight-binding Hamiltonians using high-throughput density functional theory, Scientific Data **8**, 106 (2021).

[40] G. Kresse and J. Furthmüller, Efficient iterative schemes for *ab initio* total-energy calculations using a plane-wave basis set, Phys. Rev. B **54**, 11169 (1996).

[41] G. Kresse and J. Furthmüller, Efficiency of *ab-initio* total energy calculations for metals and semiconductors using a plane-wave basis set, Comp. Mat. Sci. **6**, 15 (1996).

[42] A. Jain, S. P. Ong, G. Hautier, W. Chen, W. D. Richards, S. Dacek, S. Cholia, D. Gunter, D. Skinner, and G. Ceder, Commentary: The materials project: A materials genome approach

to accelerating materials innovation, APL Mater. **1**, 011002 (2013).

[43] https://github.com/usnistgov/jarvis.

[44] K. Choudhary, I. Kalish, R. Beams, and F. Tavazza, High-throughput identification and characterization of two-dimensional materials using density functional theory, Sci. Rep. **7**, 5179 (2017).

[45] https://jarvis.nist.gov/jarvisdft.

[46] G. Cao, H. Liu, J. Liang, L. Cheng, D. Fan, and Z. Zhang, Rhombohedral $Sb_2Se_3$ as an intrinsic topological insulator due to strong van der Waals interlayer coupling, Phys. Rev. B **97**, 075147 (2018).

[47] A. A. Mostofi, J. R. Yates, Y.-S. Lee, I. Souza, D. Vanderbilt, and N. Marzari, Wannier90: A tool for obtaining maximally-localised Wannier functions, Comp. Phys. Comm. **178**, 685 (2008).

[48] Q. Wu, S. Zhang, H.-F. Song, M. Troyer, and A. Soluyanov, WannierTools: An open-source software package for novel topological materials, Comp. Phys. Comm. **224**, 405 (2018).

[49] Please note commercial software is identified to specify procedures. Such identification does not imply recommendation by National Institute of Standards and Technology (NIST).

[50] N. Marzari and D. Vanderbilt, Maximally localized generalized Wannier functions for composite energy bands, Phys. Rev. B **56**, 12847 (1997).

[51] I. Souza, N. Marzari, and D. Vanderbilt, Maximally localized Wannier functions for entangled energy bands, Phys. Rev. B **65**, 035109 (2001).

[52] G. Ke, Q. Meng, T. Finley, T. Wang, W. Chen, W. Ma, Q. Ye, and T.-Y. Liu, LightGBM: a highly efficient gradient boosting decision tree, Adv. Neural Inf. Process. Syst. **30**, 3146 (2017).

[53] See Supplemental Material at http://link.aps.org/supplemental/10.1103/PhysRevB.103.155131 for the complete list of candidate materials and band gap comparison between different methods.

[54] K C. L. Kane and E. J. Mele, Quantum Spin Hall Effect in Graphene, Phys. Rev. Lett. **95**, 226801 (2005).

[55] F. Tran, J. Doumont, L. Kalantari, A. W. Huran, M. A. Marques, and P. Blaha, Semilocal exchange-correlation potentials for solid-state calculations: Current status and future directions, J. App. Phys. **126**, 110902 (2019).

[56] J. Nokelainen, C. Lane, R. S. Markiewicz, B. Barbiellini, A. Pulkkinen, B. Singh, J. Sun, and K. Pussi, *Ab initio* description of the $Bi_2Sr_2CaCu_2O_{8+\delta}$ electronic structure, Phys. Rev. B **101**, 214523 (2020).

[57] Y. Zhang, J. Sun, J. P. Perdew, and X. Wu, Comparative first-principles studies of prototypical ferroelectric materials by LDA, GGA, and SCAN meta-GGA, Phys. Rev. B **96**, 035143 (2017).

[58] https://jarvis.nist.gov/jarviswtb/.

[59] https://www.ctcms.nist.gov/~knc6/static/JARVIS-DFT/JVASP-8122.xml.

[60] M. Shikano, C. Delmas, and J. Darriet, $NaRuO_2$ and $Na_xRuO_2 \cdot yH_2O$: New oxide and oxyhydrate with two dimensional $RuO_2$ layers, J. Inorg. Che. **43**, 1214 (2004).

[61] M. N. Ali, L. M. Schoop, C. Garg, J. M. Lippmann, E. Lara, B. Lotsch, and S. Parkin, Butterfly magnetoresistance, quasi-2D Dirac Fermi surface and topological phase transition in ZrSiS, Sci. Adv. **2**, e1601742 (2016).

[62] C. Müller, T. Khouri, M. van Delft, S. Pezzini, Y.-T. Hsu, J. Ayres, M. Breitkreiz, L. Schoop, A. Carrington, and N. Hussey, Determination of the Fermi surface and field-induced quasiparticle tunneling around the Dirac nodal loop in ZrSiS, Phys. Rev. Res. **2**, 023217 (2020).

[63] S. Curtarolo, W. Setyawan, S. Wang, J. Xue, K. Yang, R. H. Taylor, L. J. Nelson, G. L. Hart, S. Sanvito, and M. Buongiorno-Nardelli, AFLOWLIB.ORG: A distributed materials properties repository from high-throughput *ab initio* calculations, Comput. Mat. Sci. **58**, 227 (2012).

[64] S. Kirklin, J. E. Saal, B. Meredig, A. Thompson, J. W. Doak, M. Aykol, S. Rühl, and C. Wolverton, The open quantum materials database (OQMD): Assessing the accuracy of DFT formation energies, npj Comp. Mat. **1**, 15010 (2015).

[65] G. Tenasini, E. Martino, N. Ubrig, N. J. Ghimire, H. Berger, O. Zaharko, F. Wu, J. Mitchell, I. Martin, and L. Forró, Giant anomalous Hall effect in quasi-two-dimensional layered antiferromagnet $Co_{1/3}NbS_2$, Phys. Rev. Res. **2**, 023051 (2020).

[66] S. Parkin, E. Marseglia, and P. Brown, Magnetic structure of $Co_{1/3}NbS_2$ and $Co_{1/3}TaS_2$, J. Physics C: Solid State Physics **16**, 2765 (1983).

[67] H. Yang, Y. Sun, Y. Zhang, W.-J. Shi, S. S. Parkin, and B. Yan, Topological Weyl semimetals in the chiral antiferromagnetic materials $Mn_3Ge$ and $Mn_3Sn$, New J. Phys. **19**, 015008 (2017).

[68] H. Tsai, T. Higo, K. Kondou, T. Nomoto, A. Sakai, A. Kobayashi, T. Nakano, K. Yakushiji, R. Arita, and S. Miwa, Electrical manipulation of a topological antiferromagnetic state, Nature **580**, 608 (2020).

[69] Y. Chen, J. Gaudet, S. Dasgupta, G. Marcus, J. Lin, T. Chen, T. Tomita, M. Ikhlas, Y. Zhao, and W. Chen, Antichiral spin order, its soft modes, and their hybridization with phonons in the topological semimetal $Mn_3Ge$, Phys. Rev. B **102**, 054403 (2020).